Research Square

Preprints are preliminary reports that have not undergone peer review.
They should not be considered conclusive, used to inform clinical practice,
or referenced by the media as validated information.

Synergistic Dual-Plasticizer Engineering of Gel Polymer Electrolytes for Accelerated Zn^{2+} Transport and Stable Zinc Deposition

Sreshtha Ganguly
Indian Institute of Technology Kharagpur
Dilip Bennada
Indian Institute of Technology Kharagpur
Amrit Choudhury
Indian Institute of Technology Kharagpur
Sreeraj Puravankara
sreeraj@iitkgp.ac.in
Indian Institute of Technology Kharagpur

Article

Keywords: Gel polymer electrolytes, Dual plasticizer, Aqueous zinc-ion battery, Zn deposition, Propylene carbonate, Glycerol

Posted Date: August 12th, 2026

DOI: https://doi.org/10.21203/rs.3.rs-10525480/v1

License: This work is licensed under a Creative Commons Attribution 4.0 International License.
Read Full License

Additional Declarations: No competing interests reported.

Synergistic Dual-Plasticizer Engineering of Gel Polymer Electrolytes for Accelerated Zn^{2+} Transport and Stable Zinc Deposition

Sreshtha Ganguly[1], Dilip Bennada[1], Amrit Choudhury[1], Sreeraj Puravankara[1*]

[1]School of Energy Science and Engineering, Indian Institute of Technology Kharagpur, Kharagpur, West Bengal 721302, India

*Email: sreeraj@iitkgp.ac.in

Phone: +91(0)3222 260801

Abstract

Gel polymer electrolytes (GPEs) have emerged as promising alternatives to liquid electrolytes for aqueous zinc-ion batteries (AZIBs); however, achieving both high ionic conductivity and stable Zn deposition simultaneously remains a significant challenge. Herein, we report a dual-plasticizer engineering strategy by incorporating propylene carbonate (PC) and glycerol into a citric acid-crosslinked carboxymethyl cellulose (CMC) GPE. The synergistic plasticization effect reduces polymer crystallinity, increases interchain spacing, and enhances electrolyte uptake, resulting in an ionic conductivity of 9.06 mS cm^{-1} and a Zn^{2+} transference number of 0.97. Consequently, the optimized electrolyte promotes rapid Zn nucleation, lowers interfacial resistance, and enables homogeneous Zn^{2+} transport, leading to uniform Zn deposition. Zn|Zn symmetric cells exhibit stable cycling for approximately 2500 hours, while Zn|V_2O_5 full cell maintains stable operation for 1000 cycles at 1 A g^{-1}. The enhanced electrochemical performance stems from the complementary roles of PC in facilitating $ZnSO_4$ dissociation and of glycerol in enhancing polymer chain mobility, thereby simultaneously optimizing ion transport and Zn/electrolyte interfacial stability. This work establishes dual-plasticizer engineering as a simple and effective strategy for designing high-performance GPEs for durable AZIBs.

Keywords: Gel polymer electrolytes, Dual plasticizer, Aqueous zinc-ion battery, Zn deposition, Propylene carbonate, Glycerol

Introduction

Aqueous zinc-ion batteries (AZIBs) have emerged as promising candidates for next-generation energy storage owing to their intrinsic safety, low cost, environmental benignity, and the high theoretical capacity of metallic Zn.[1–5] However, conventional aqueous electrolytes suffer from parasitic side reactions, including hydrogen evolution, Zn corrosion, and dendritic Zn growth, which lead to poor cycling stability and limit their practical application. Gel polymer electrolytes (GPEs) have therefore attracted considerable attention because they integrate the high ionic conductivity of liquid electrolytes with the mechanical robustness, leakage resistance, and interfacial stability of solid electrolytes, thereby offering an effective strategy for regulating Zn deposition and improving battery safety.[6]

Among the various polymer matrices investigated for GPEs, naturally derived polymers have received increasing attention owing to their sustainability, low cost, biodegradability, and abundant functional groups.[7–9] In particular, carboxymethyl cellulose (CMC) is an attractive host polymer because of its excellent film-forming ability, hydrophilicity, and strong affinity toward aqueous electrolytes.[10,11] However, further enhancement of the ionic transport properties of CMC-based GPEs remains essential to achieve stable Zn deposition and improved electrochemical performance. In this regard, plasticizer engineering has emerged as an effective strategy for tailoring the physicochemical properties of polymer electrolytes. Plasticizers reduce polymer–polymer interactions, increase the amorphous fraction, and lower the glass transition temperature, thereby enhancing polymer segmental mobility, facilitating salt dissociation, and improving ion transport.[12,13] Consequently, the ionic conductivity of GPEs is strongly influenced by the physicochemical properties of the plasticizer, particularly its dielectric constant, molecular structure, and interactions with the polymer matrix. Since different plasticizers possess distinct

physicochemical characteristics, mixtures of plasticizers are often employed to combine their complementary advantages.[14] For instance, Zuo et al. reported that incorporating poly(ethylene glycol) dimethyl ether (PEGDME) and poly(ethylene glycol) dilaurate (PEGDL) as dual plasticizers significantly enhanced the mechanical properties and ionic conductivity of GPEs in lithium-ion batteries (LIBs).[15] Likewise, Liu et al. reported enhanced ionic conductivity and electrochemical performance using a mixed ethylene carbonate (EC)/ diethyl carbonate (DEC) plasticizer system in PVDF-HFP GPEs for LIBs.[16] Gohel and Kanchan demonstrated that a propylene carbonate (PC)/DEC plasticizer system significantly improved the structural and electrical properties of PVDF-HFP/PMMA GPEs.[17] Despite these encouraging advances, dual-plasticizer engineering has been explored predominantly in lithium-based electrolytes[18], whereas its application to zinc-based GPEs remains largely unexplored.

Herein, we address this gap by developing a citric acid-crosslinked CMC GPE incorporating PC and glycerol as dual plasticizers for aqueous zinc-ion batteries. Their complementary physicochemical characteristics guided the selection of PC and glycerol. PC, with its high dielectric constant ($\varepsilon \approx 66$)[14], effectively promotes $ZnSO_4$ dissociation and increases the concentration of mobile charge carriers. Complementing the role of PC, glycerol is a highly hydrophilic trihydric alcohol whose three hydroxyl groups establish extensive hydrogen-bonding interactions with the polymer matrix, thereby enhancing polymer flexibility, electrolyte affinity, and segmental mobility.[19,20] The optimized electrolyte exhibits high ionic conductivity, enhanced Zn^{2+} transference, and reduced interfacial resistance, enabling uniform Zn deposition and stable electrochemical performance in both Zn|Zn symmetric and Zn|V_2O_5 full cells. This work demonstrates dual-plasticizer engineering as a simple and effective strategy for designing high-performance GPEs for durable AZIBs.

Experimental Methods

Materials

Sodium carboxymethyl cellulose (CAS: 9004-32-4, MW =250,000, degree of substitution = 1.2), zinc sulfate heptahydrate (ACS reagent, 99%), polyvinylidene fluoride (PVDF) (MW =534,000), copper foil (0.025 mm), and propylene carbonate (>99%) were purchased from Sigma-Aldrich, Mumbai, India. Citric acid monohydrate, N-methyl-2-pyrrolidone (NMP) (99%), and Glycerol (99%) were purchased from Loba Chemie, Mumbai, India. Vanadium oxide (V_2O_5) (>98%) was purchased from TCI Chemicals, Hyderabad, India. Zinc foil (0.1 mm) was purchased from Global Nanotech, India, and was polished to eliminate any unwanted surface layers. It was then washed using a mixture of acetone and isopropyl alcohol. Conductive carbon (Super P) and stainless steel (SS-316) mesh were procured and used directly without any prior treatment.

Preparation of the gel polymer electrolyte

To prepare the gel polymer electrolyte (GPE), 4.5 wt% citric acid (CA) was first dissolved in de-ionized water and heated in a hot bath at 95°C. Citric acid acts as a cross-linking agent, enhancing the structural integrity and mechanical stability of the GPE.[21] Sodium carboxymethyl cellulose (NaCMC) (10 wt%) was then added to the CA solution and stirred manually for 1 hour at 90°C to achieve a homogeneous mixture. Subsequently, the plasticizer solutions, consisting of propylene carbonate (PC) and glycerol in varying ratios, were added to the mixture, which was then stirred for 30 minutes. The resulting solutions were centrifuged to remove air bubbles before being cast onto Petri dishes. The membranes were dried at room temperature overnight, then dried at 50°C for 4 hours.

For convenience, the cross-linked membranes are denoted as PGxy, where "P" represents PC, "G" represents glycerol, and x and y indicate the respective weight percentages of PC and glycerol in the formulation.

To obtain the final GPE, 19-mm discs were cut from the dried membranes and soaked in a 3 M $ZnSO_4$ solution for 24 hours. All the experiments were carried out with 3M $ZnSO_4$ unless stated otherwise. For PG00, the CMC-CA solution was directly subjected to centrifugation and solution casting without adding any plasticizer. The dried membranes were stored in a desiccator until further experimentation.

Preparation of the plasticizer solutions

A 10 wt% plasticizer solution, with respect to the CMC-CA mixture, was prepared in a beaker and stirred for 10 minutes. The compositions for different formulations are presented in the table below (Table 1):

Table 1. **Formulation and plasticizer ratios of CMC-based GPEs.:** GPE membrane compositions for the as-synthesized GPEs with varying PC and glycerol ratios.

Formulation	PC content (wt%)	Glycerol content (wt%)
PG00	0	0
PG10	10	0
PG11	5	5
PG01	0	10

Preparation of V_2O_5 cathode

The cathode was prepared by uniformly mixing vanadium pentoxide (V_2O_5), Super P, and polyvinylidene fluoride (PVDF) in a 7:2:1 weight ratio using N-methyl-2-pyrrolidone (NMP) as the solvent. The resulting slurry was coated onto a stainless steel (SS) mesh with a diameter of 15 mm and dried under vacuum at 120°C overnight. The areal loading of active V_2O_5 was approximately 4 mg cm^{-2}.

Characterizations

The electrolyte absorption ability (η) of the GPE membranes was evaluated by immersing the membranes in a 3 M $ZnSO_4$ solution for 24 hours. The initial weight (Wi) before soaking and the weight (Wa) after soaking were recorded, and η was determined using equation (1)[22]:

$$\eta = \frac{Wa - Wi}{Wi} \, x \, 100\% \qquad (1)$$

The mechanical properties of the membranes were evaluated at room temperature using a universal testing machine (Zwick Roell) equipped with a 100 N load cell, with 5 cm × 0.5 cm membrane strips. Surface and cross-sectional morphologies were examined using field-emission scanning electron microscopy (FESEM, MERLIN, Zeiss Gemini 2) operated at 10 kV after drying the membranes at 55 °C for 24 h and sputter-coating them with gold. Surface topography was further investigated using atomic force microscopy (AFM, Agilent 5500) with a probe having a resonance frequency of 150 kHz and a spring constant of 1 N m^{-1}. X-ray diffraction (XRD) patterns were recorded on a Bruker D2 Phaser diffractometer using Cu Kα radiation (λ = 1.5418 Å). Thermogravimetric analysis (TGA) was carried out on a PerkinElmer Pyris Diamond instrument under a nitrogen atmosphere from 40 to 800 °C at a heating rate of 12 °C min^{-1}. The viscosity of

$ZnSO_4$ solutions at different concentrations was measured at room temperature using a BDV-8S digital viscometer.

Electrochemical Measurements

The voltage stability windows of the GPE membranes were analyzed using linear sweep voltammetry (LSV) with a Zn|SS battery configuration. The potential was varied from 0 to 2.5 V at a sweep rate of 0.5 mV sec^{-1}. Additionally, cyclic voltammetry (CV) was performed on the Zn|SS battery system over the potential range of -0.25 V to 1.1 V at a scan rate of 0.5 mV s^{-1}. The ionic conductivities of the GPE membranes at room temperature were measured using a stainless-steel blocking cell with electrochemical impedance spectroscopy (EIS) over the frequency range of 10 kHz to 1 Hz, applying a 10 mV AC signal. Ionic conductivity (σ) was calculated using equation (2)[23,24], where *l* is the thickness of the GPE membranes, *R* is the resistance obtained from the X-axis intercept of the Nyquist plot, and *A* is the contact area between the membrane and the electrodes.

$$\sigma \text{ (mS cm}^{-1}) = \frac{l}{R \, x \, A} \qquad (2)$$

The zinc-ion transference number ($t_{Zn^{2+}}$) for the membranes was also determined using the Bruce-Vincent-Evans method. A zinc symmetric battery configuration (Zn|Zn) with DC polarization was used, and $t_{Zn^{2+}}$ was calculated using equation (3)[25]where Io and Is are the initial and steady-state currents, ΔV is the step potential, and Ro and Rs are the resistances before and after polarization.

$$Transference\ number = \frac{Is\ (\Delta V - IoRo)}{Io\ (\Delta V - IsRs)} \qquad (3)$$

To investigate the Zn deposition behavior and Zn^{2+} diffusion characteristics, chronoamperometric measurements were performed on Zn|Zn symmetric cells containing PG00 and PG11 under a constant polarization of −100 mV. The reversibility of zinc plating/stripping was studied in symmetric Zn|Zn and asymmetric Zn|Cu battery configurations using a constant-current cycling technique with the NEWARE testing system. The experiments were conducted at a current density of 1 mA cm^{-2} and a specific capacity of 1 mAh cm^{-2}. Zn|Zn symmetric cells were cycled at a current density of 5.6 mA cm^{-2} and an areal capacity of 28.3 mAh cm^{-2}, corresponding to 50% depth of discharge (DOD). The DOD was calculated using equation (4), where I is the current density, t is the plating/stripping time, m is the mass of the Zn electrode, and A is the theoretical capacity of Zn.

$$DOD\ (\%) = \frac{It}{mA} * 100 \qquad (4)$$

Chrono-amperometry measurements were conducted for Zn|Zn symmetric cells at a fixed potential of -100 mV to investigate zinc diffusion on the surface of the zinc anode. EIS measurements were performed on Zn|Cu cells with a 10 mV AC amplitude under open-circuit voltage (OCV) and biased conditions corresponding to the initial Zn nucleation overpotential. The full cells (coin cells CR-2032) were constructed with polished Zn as the anode and V_2O_5 as the cathode. The charge-discharge behaviors were analyzed by cycling these cells at constant current densities of 0.1 A g^{-1} and 1 A g^{-1} using a Bio-Logic battery cycler. The rate performance of the full cells was evaluated by cycling them at varying current densities of 0.2 A g^{-1}, 0.5 A g^{-1}, 1 A g^{-1}, and 2 A g^{-1} for five cycles each, followed by a return to 0.2 A g^{-1}. Before this, the cells were cycled for 30 cycles at 0.2 A g^{-1} to activate the cathode.

Results & Discussion

Figure 1a schematically illustrates the fabrication process of the citric acid-crosslinked NaCMC gel polymer electrolyte incorporating propylene carbonate and glycerol as plasticizers.

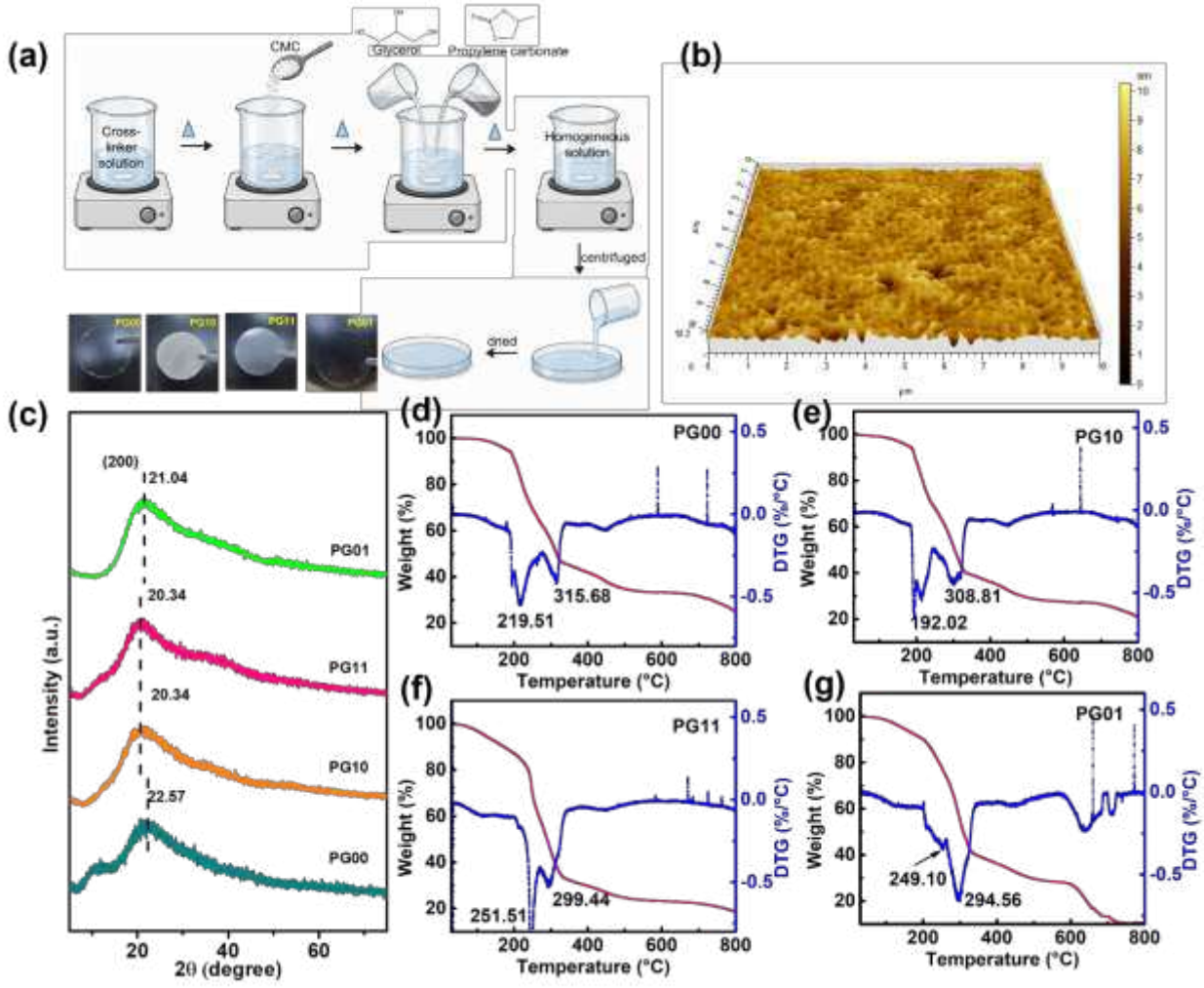


Figure 1. **Structural, morphological, and thermal evolution of CMC-based gel polymer electrolytes:** (a) Schematic illustration of the fabrication process of the CMC-based GPEs containing different PC and glycerol compositions (PG00, PG10, PG11, and PG01); (b) Three-dimensional AFM surface topography of PG11 membrane; (c) XRD patterns of the GPEs; TG and DTG curves of (d) PG00, (e) PG10, (f) PG11, and (g) PG01.

The combined plasticization strategy was adopted to simultaneously enhance polymer chain flexibility and electrolyte affinity while preserving the structural integrity imparted by the crosslinked NaCMC network. The three-dimensional AFM topographical image of PG11 membrane (Figure 1b) exhibits a continuous and homogeneous surface with uniformly distributed nanoscale features and no discernible cracks, confirming the formation of a well-integrated gel polymer electrolyte. The cross-sectional SEM image of the pristine membrane (Figure S1a) reveals a free-standing film with a uniform thickness of approximately 128 μm, indicating successful membrane formation through the solution-casting process. The surface morphologies of PG00, PG10, PG11, and PG01 are presented in Figures S1b-e. All membranes exhibit a continuous porous architecture. The incorporation of PC and glycerol modifies the pore morphology, resulting in a more open and interconnected structure than PG00. Such morphological evolution is expected to facilitate electrolyte infiltration. The structural characteristics of the prepared GPEs were investigated by XRD, and the corresponding diffraction patterns are presented in Figure 1c. All membranes exhibit a broad diffraction halo centered at 20-23°, corresponding to the (200) reflection of NaCMC[26], indicative of the predominantly amorphous nature of the crosslinked polymer matrix. Upon incorporation of the plasticizers, the (200) peak shifts from 22.57° for PG00 to lower angles of 20.34° for both PG10 and PG11, and 21.04° for PG01. Consequently, the calculated average interchain distance (<R>)[27] increases from 4.91 Å for PG00 to 5.45 Å for both PG10 and PG11, while PG01 exhibits an intermediate value of 5.27 Å (Table S1a), confirming that the plasticizer molecules effectively expand the polymer chain spacing and weaken intermolecular interactions. To further quantify the structural changes, the diffraction profiles were deconvoluted into crystalline and amorphous contributions (Figure S2), and the corresponding degree of crystallinity was calculated (Table S1b).[28,29] The crystallinity decreases markedly from

81.54% for PG00 to 62.50% for PG10 and further to 59.93% for PG11, whereas PG01 retains a comparatively higher crystallinity of 77.97%. The reduced crystallinity, together with the enlarged interchain spacing, demonstrates that dual plasticization effectively disrupts polymer chain ordering, enhances the amorphous character of the membrane, and is expected to promote segmental mobility of polymers and facilitate Zn^{2+} transport in the gel electrolyte. The thermal stability of the prepared GPEs was evaluated by TGA and DTG, as shown in Figures 1d-g. All membranes exhibit two distinct weight-loss regions. The initial weight loss below approximately 250 °C is attributed to the evaporation of physically adsorbed and bound water entrapped within the hydrophilic NaCMC network. The second decomposition event, observed between ~250 and 350 °C, corresponds to the degradation of the crosslinked polymer backbone.[30] The DTG curves reveal slight variations in the maximum degradation temperature with plasticizer composition,

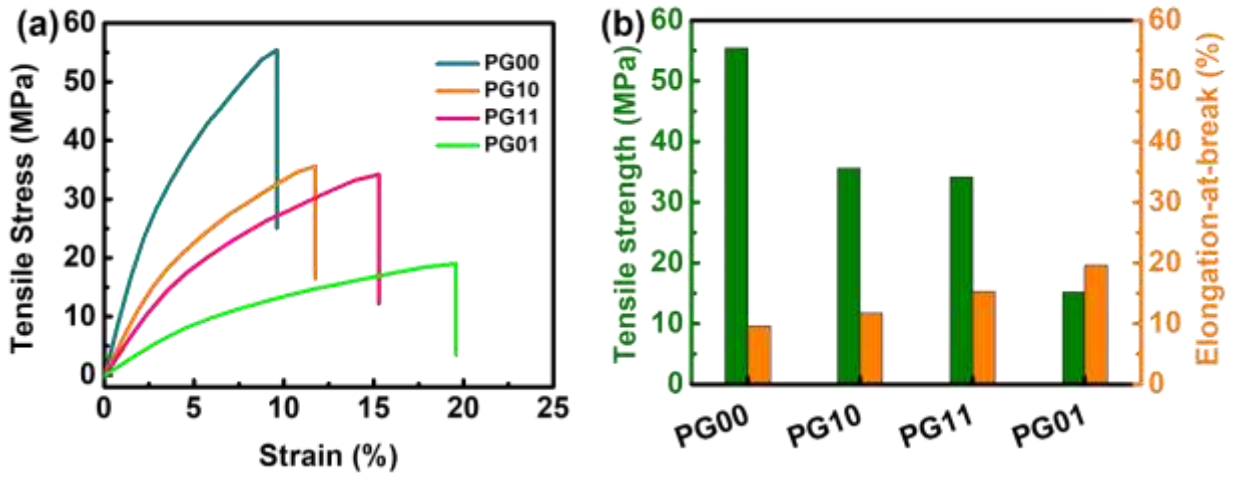


Figure 2. **Tensile behavior and mechanical flexibility of CMC-based GPEs:** Mechanical properties of the GPE membranes. (a) Representative stress-strain curves of PG00, PG10, PG11, and PG01; (b) Comparison of the tensile strength and elongation-at-break of the prepared GPE membranes.

indicating that the incorporation of PC and glycerol alters the intermolecular interactions within the polymer network without significantly affecting its overall thermal stability. Notably, all membranes remain thermally stable well above the operating temperatures of AZIBs, confirming that dual plasticization preserves the thermal robustness required for practical electrolyte applications.

The mechanical properties of the prepared membranes were evaluated by tensile testing; the corresponding stress-strain curves are shown in Figure 2a, and the tensile strength and elongation at break are summarized in Figure 2b. The pristine membrane (PG00) exhibits the highest tensile strength, approximately 55 MPa, and an elongation at break of 9%, reflecting the rigid nature of the crosslinked NaCMC network. Upon incorporation of the plasticizers, the tensile strength decreases to 35 MPa (PG10), 34 MPa (PG11), and 15 MPa (PG01), accompanied by an increase in elongation at break to 11%, 14%, and 19%, respectively. The enhanced flexibility is attributed to the plasticizers weakening the intermolecular hydrogen-bonding interactions between polymer chains, thereby increasing chain mobility. Compared with PC, glycerol exhibits a stronger plasticization effect, as evidenced by the higher elongation and lower tensile strength of PG01. Meanwhile, the dual-plasticized PG11 membrane achieves a balance between mechanical strength and flexibility, which is desirable for maintaining membrane integrity during battery assembly and operation.

The electrolyte uptake of the prepared GPEs is presented in Figure 3a and Table S2. The electrolyte uptake increased significantly from 76% for PG00 to 109%, 172%, and 143% for PG10, PG11, and PG01, respectively. The enhanced uptake is attributed to the plasticizer-induced increase in interchain spacing, together with the development of a more open and interconnected porous structure

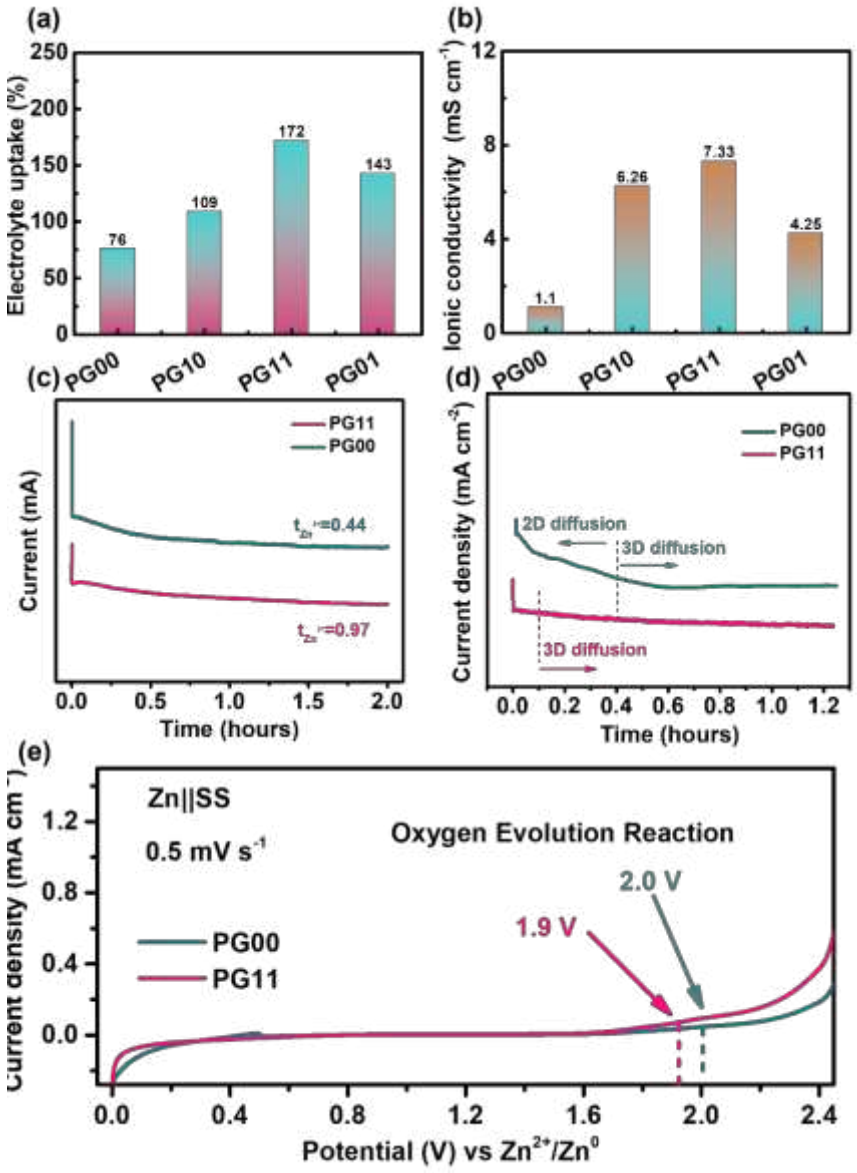


Figure 3. **Enhanced ion transport kinetics and electrochemical window of GPEs:** (a) Electrolyte uptake of PG00, PG10, PG11, and PG01 after soaking in 3 M $ZnSO_4$ electrolyte; (b) Ionic conductivity of the prepared GPEs at room temperature; (c) Zn^{2+} transference number measurements of PG00 and PG11 using the Bruce–Vincent method; (d) Chronoamperometric response of Zn|Zn symmetric cells at a polarization of -100 mV, illustrating the Zn^{2+} diffusion behavior in PG00 and PG11; (e) LSV of Zn|SS cells at a scan rate of 0.5 mV s^{-1}.

morphology observed in the SEM images, which collectively facilitate electrolyte infiltration and retention within the polymer matrix. Among all the membranes, PG11 exhibited the highest electrolyte uptake, indicating a synergistic effect between PC and glycerol in enhancing electrolyte affinity. To further understand the interaction between the gel polymer matrix and the absorbed electrolyte, the $ZnSO_4$-soaked membranes were characterized by XRD and SEM after drying (Figure S3a-e). The plasticized membranes (PG10, PG11, and PG01) retain broad amorphous diffraction halos without discernible reflections corresponding to crystalline $ZnSO_4$, indicating homogeneous incorporation of the electrolyte within the polymer network and suppression of salt recrystallization upon drying. In contrast, the soaked PG00 membrane exhibits several sharp diffraction peaks along with visible crystalline deposits in the SEM image, suggesting localized $ZnSO_4$. Conversely, the plasticized membranes display comparatively uniform surfaces without obvious crystalline salt aggregates, particularly PG11, reflecting more homogeneous electrolyte distribution. The improved electrolyte accommodation afforded by plasticization, together with the high dielectric constant of PC, which facilitates $ZnSO_4$ dissociation, and the enhanced polymer chain mobility imparted by glycerol, provides a larger population of mobile Zn^{2+} charge carriers. The ionic conductivities of the prepared GPEs are presented in Figures 3b and Table S3, and the corresponding Nyquist plots used for conductivity measurements are presented in Figure S4a. The ionic conductivity values were 1.10, 6.26, 7.33, and 4.25 mS cm^{-1} for PG00, PG10, PG11, and PG01, respectively, demonstrating the superior ion-transport capability of the dual-plasticized PG11 membrane. The remarkable enhancement in ionic conductivity is attributed to the combined effects of increased polymer segmental mobility and higher electrolyte uptake, which facilitate Zn^{2+} migration through the gel matrix. While glycerol enhances polymer flexibility, PC promotes efficient salt dissociation owing to its high dielectric constant. The synergistic combination of

these two plasticizers in PG11 therefore provides an optimal balance between polymer flexibility and ionic transport, resulting in the highest electrolyte uptake and ionic conductivity. Consequently, PG11 was selected as the optimized GPE for all subsequent electrochemical investigations. For the optimized PG11 membrane, the $ZnSO_4$ concentration was further optimized by balancing electrolyte uptake, solution viscosity, and ionic conductivity (Figures S4b-d and Tables S4a-c). The ionic conductivity increased with salt concentration, reaching a maximum of 9.06 mS cm^{-1} at 3 M $ZnSO_4$, then declined at higher concentrations due to increased solution viscosity. Therefore, 3 M $ZnSO_4$ was selected for all subsequent electrochemical investigations. The Zn^{2+} transference number was determined using the Bruce-Vincent method, and the corresponding chronoamperometric responses are presented in Figure 3c. The Nyquist plots recorded before and after polarization, together with the calculated parameters, are provided in Figure S5a, b and Table S5, respectively. PG11 exhibits a higher Zn^{2+} transference number of 0.97 compared to 0.44 for PG00, indicating that Zn^{2} ions carry a larger fraction of the ionic current in the dual-plasticized electrolyte. The enhanced cation transport is attributed to the synergistic effect of PC and glycerol, in which PC's high dielectric constant promotes $ZnSO_4$ dissociation. In contrast, glycerol enhances polymer segmental mobility, thereby facilitating preferential Zn^{2+} migration. The Zn^{2+} diffusion behavior[31,32] was further investigated, and the corresponding chronoamperogram is shown in Figure 3d. PG00 exhibits a prolonged 2D diffusion regime lasting approximately 24 min, after which the diffusion gradually transitions to a 3D mode. In contrast, PG11 undergoes a much earlier transition from 2D to 3D diffusion within approximately 6 min, reflecting more homogeneous Zn^{2+} flux at the electrode-electrolyte interface. Consequently, the higher Zn^{2+} transference number and accelerated diffusion kinetics of PG11 are expected to promote uniform zinc deposition and suppress dendrite growth. The electrochemical stability

window of the GPES was evaluated by LSV using Zn||SS cells at a scan rate of 0.5 mV s^{-1} (Figure 3e). Both electrolytes exhibit negligible anodic current over a wide potential range, indicating good electrochemical stability. The onset of oxygen evolution occurs at approximately 2.0 V for PG00 and 1.9 V for PG11. The slightly earlier onset observed for PG11 can be attributed to its higher electrolyte uptake and increased availability of water molecules within the plasticized gel network, which facilitates the oxygen evolution reaction. Nevertheless, both electrolytes provide a sufficiently wide electrochemical stability window for AZIB operation, confirming that dual plasticization does not compromise the GPE's electrochemical stability.

The Zn plating/stripping reversibility of the optimized GPE was evaluated using Zn|Zn symmetric cells at a current density and areal capacity of 1 mA cm^{-2} and 1 mAh cm^{-2}, respectively (Figure 4a). For comparison, the initial cycling behavior of PG00 and PG11 is presented in Figure S6a. The PG00 cell exhibits pronounced voltage fluctuations, indicating unstable Zn deposition/stripping and non-uniform Zn growth. In contrast, PG11 displays highly stable and symmetric voltage profiles with a low polarization of approximately 0.1 V, demonstrating highly reversible Zn plating/stripping. During extended cycling, the PG11 cell maintains stable operation for approximately 2500 hours with negligible increase in polarization, highlighting the excellent long-term interfacial stability of the dual-plasticized electrolyte. Conversely, the PG00 cell undergoes a sharp increase in overpotential after approximately 1135 hours, followed by severe voltage fluctuations, indicative of interfacial degradation and dendrite-induced cell failure. The outstanding cycling stability of PG11 is attributed to its superior ionic conductivity, higher Zn^{2+} transference number, and accelerated ion transport kinetics, which collectively ensure a homogeneous Zn^{2+} flux and promote uniform zinc deposition. At 50% DOD, the PG11 symmetric cell exhibits stable Zn plating/stripping over more than 400 hours (Fig. S6b).

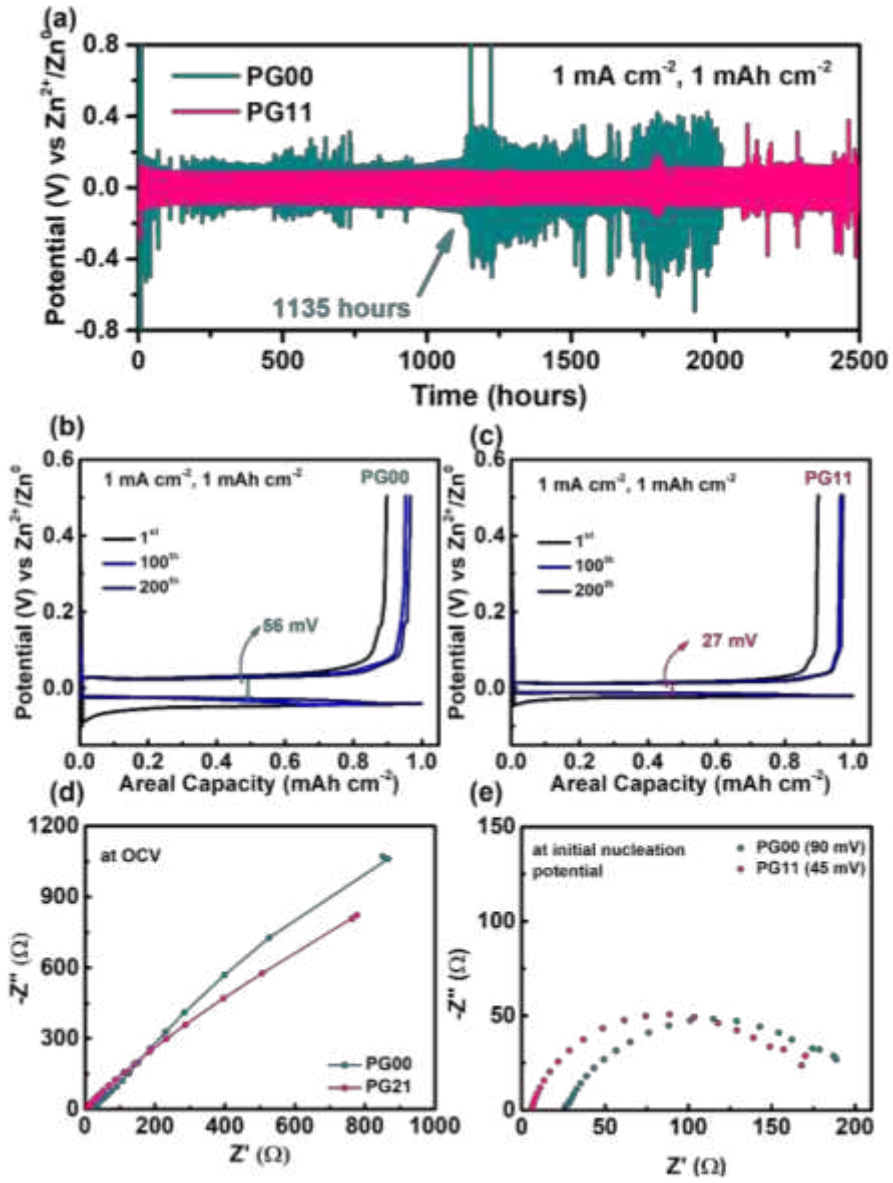


Figure 4. **Reversibility and interfacial kinetics of Zn plating/stripping:** (a) Long-term Zn plating/stripping performance of Zn|Zn symmetric cells using PG00 and PG11 at 1 mA cm^{-2} with an areal capacity of 1 mAh cm^{-2}; Zn nucleation overpotential of Zn|Cu cells during the 1st, 100th, and 200th plating cycles at 1 mA cm^{-2} and 1 mAh cm^{-2} for (b) PG00, and (c) PG11; EIS spectra of Zn|Cu cells measured under (d) OCV; and (e) an applied bias corresponding to the initial Zn nucleation overpotential.

The Zn plating/stripping behavior was further investigated using Zn|Cu cells at a current density of 1 mA cm^{-2} and an areal capacity of 1 mAh cm^{-2} (Figures 4b, c). The voltage profiles recorded during the 1st, 100th, and 200th cycles reveal excellent cycling reversibility for both electrolytes. However, PG11 exhibits a substantially lower Zn nucleation overpotential of 27 mV compared to 56 mV for PG00, indicating a reduced energy barrier for Zn nucleation. Figure S6c presents the coulombic efficiency of the Zn|Cu cells, with both PG00 and PG11 maintaining an average coulombic efficiency of approximately 99% over 200 cycles. The cyclic voltammograms shown in Figure S7a reveal an earlier cathodic onset for PG11 than PG00, indicating faster Zn nucleation kinetics.[33] and improved Zn^{2+} transport in the dual-plasticized gel electrolyte.

To elucidate the interfacial charge-transfer characteristics during Zn nucleation, EIS was performed on Zn|Cu cells under OCV and biased conditions, with the bias set to the respective initial Zn nucleation overpotential. The nucleation overpotentials were first determined from the initial Zn plating profiles of Zn|Cu cells (Figure S7b, c), yielding values of 45 mV for PG11 and 90 mV for PG00. These respective potentials were subsequently applied as the bias potentials for EIS measurements. The Nyquist plots recorded at OCV and under biased conditions are presented in Figures 4d and 4e, respectively. At the same time, the fitted impedance parameters and equivalent circuit models are summarized in Table S6 and Figures S7d and S7c. At OCV, PG11 exhibits a significantly lower solution resistance (R_s = 4.13 Ω) than PG00 (22.58 Ω), consistent with its higher ionic conductivity. Upon polarization to the Zn nucleation potential, the impedance spectra display distinct interfacial processes associated with Zn electrodeposition. The fitted results reveal that PG11 exhibits substantially lower interfacial resistance (RSEI = 86.99 Ω) and charge-transfer resistance (Rct = 90.67 Ω) than PG00 (R_{SEI} = 159.5 Ω and Rct = 305.4 Ω). These results indicate that the dual-plasticized electrolyte facilitates rapid Zn^{2+} de-solvation and charge

transfer at the electrode-electrolyte interface, thereby reducing the nucleation energy barrier and enabling more uniform Zn deposition. The reduced interfacial impedance is in excellent agreement with the lower nucleation overpotential, higher Zn^{2+} transference number, improved diffusion kinetics, and superior long-term cycling stability observed for PG11. To further correlate these electrochemical improvements with the morphology of Zn deposition, the Zn electrodes after cycling were examined by SEM. The morphology of Zn anodes retrieved from Zn\Zn symmetric cells after prolonged cycling was examined to elucidate the influence of the electrolyte on Zn deposition behavior (Figures 5a, b). After 200 cycles, the Zn anode cycled with PG00 exhibits a rough and irregular surface, indicative of non-uniform Zn deposition. In contrast, the Zn anode cycled with PG11 retains a compact and smooth morphology with uniformly distributed Zn deposits and no discernible dendritic features, demonstrating its ability to promote homogeneous Zn deposition during repeated cycling. Based on the above experimental findings, a schematic illustration of the proposed Zn^{2+} transport mechanism is presented in Figure 5c. The synergistic effect of the two plasticizers promotes efficient Zn^{2+} transport through the polymer network, resulting in a more homogeneous Zn^{2+} flux at the electrode/electrolyte interface. Consequently, uniform Zn plating/stripping with reduced interfacial resistance is achieved, consistent with the stable long-term cycling, low polarization, and compact Zn deposition observed experimentally.

The practical applicability of the optimized GPE was further evaluated in Zn|V_2O_5 full cells. The GCD voltage-capacity profiles of the PG11-based Zn|V_2O_5 full cell at 0.1 and 1 A g^{-1} are shown in Figures S8a, b, respectively. At a current density of 0.1 A g^{-1} (Figure 5d), the cell delivers a maximum discharge capacity of approximately 280 mAh g^{-1}. It retains 241 mAh g^{-1} after 300 cycles, corresponding to ~86% capacity retention, while maintaining an average coulombic efficiency of ~96%.

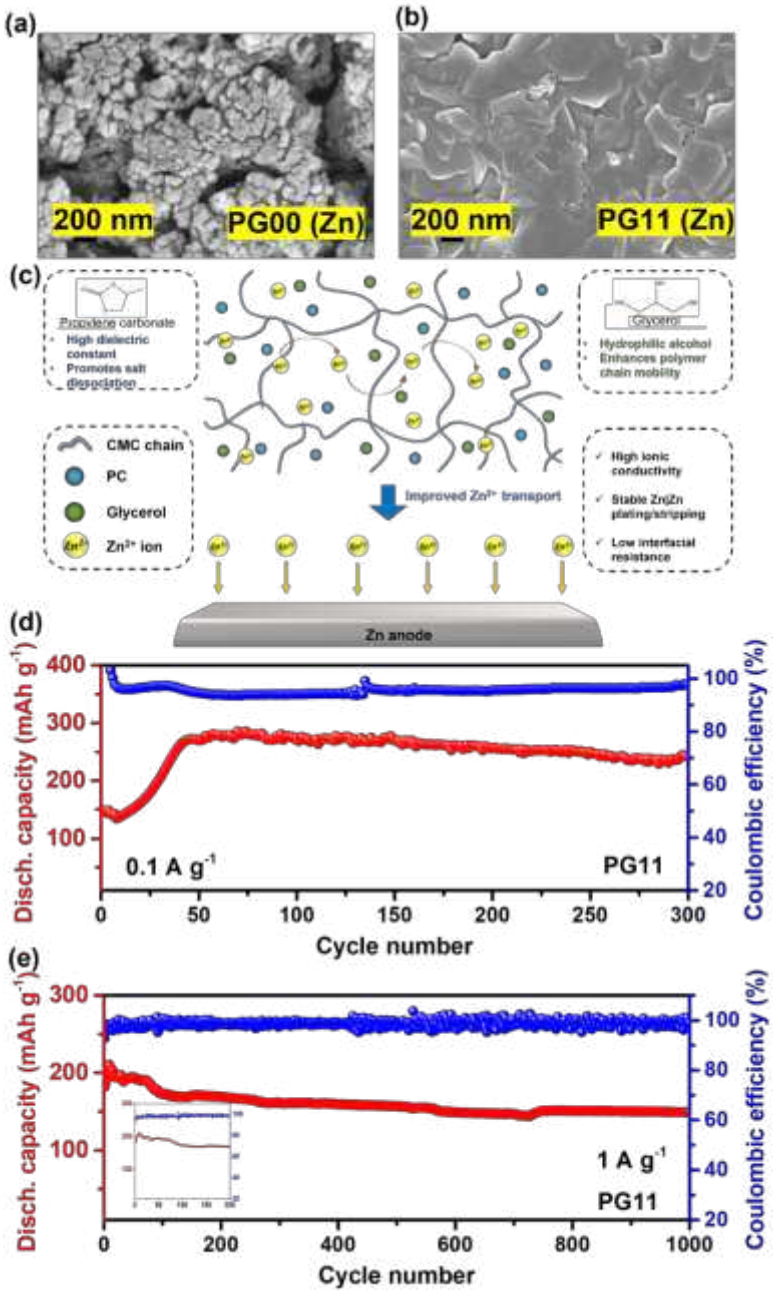


Figure 5. **Morphological evolution, transport mechanism, and full-cell performance of GPEs:** Post-cycling SEM images of Zn anodes retrieved from Zn|Zn symmetric cells after 200 cycles, using (a) PG00, and (b) PG11; (c) Proposed Zn^{2+} transport mechanism in the dual-plasticized GPE; Cycling performance and coulombic efficiency of Zn|V_2O_5 full cells with the PG11 electrolyte at (d) 0.1 A g^{-1}, and (e) 1 A g^{-1}.

An initial increase in the discharge capacity is observed during the early cycles, which can be attributed to the electrochemical activation of the pristine V_2O_5 cathode into $Zn_xV_2O_5{\cdot}nH_2O$. This activated phase provides additional Zn^{2+} insertion/extraction sites and an expanded interlayer spacing, facilitating improved Zn^{2+} storage.[34] Even at a higher current density of 1 A g^{-1} (Figure 5e), the cell exhibits excellent cycling stability, delivering an initial discharge capacity of approximately 210 mAh g^{-1} and retaining 149 mAh g^{-1} after 1000 cycles, corresponding to a capacity retention of ~71%, with an average coulombic efficiency of approximately ~98%. A similar initial capacity increase is also observed at 1 A g^{-1}, indicating the same cathode activation process. The stable cycling performance under both low- and high-rate conditions demonstrates the excellent interfacial compatibility and electrochemical stability of the dual-plasticized GPE. Furthermore, the rate capability (Figure S8c) shows that PG11 consistently delivers higher discharge capacities than PG00 across all investigated current densities and fully recovers its initial capacity upon returning to 0.2 A g^{-1}, indicating excellent rate reversibility. To demonstrate its practical feasibility, three $Zn|V_2O_5$ coin cells connected in series delivered a combined OCV of 2.77 V and successfully powered light-emitting diodes (LEDs) of different colors (Figure S9), highlighting the potential of the optimized GPE for practical AZIB applications.

Conclusion

In summary, we demonstrate a simple yet effective dual-plasticizer engineering strategy for CMC-based GPEs by synergistically combining PC and glycerol to enhance Zn^{2+} transport and interfacial stability in aqueous zinc-ion batteries. The optimized PG11 electrolyte exhibits high ionic conductivity (9.06 mS cm^{-1}) and a Zn^{2+} transference number of 0.97, arising from improved electrolyte uptake, reduced polymer crystallinity, and enhanced polymer chain mobility. Consequently, the electrolyte enables rapid Zn nucleation, low interfacial resistance, homogeneous

Zn deposition, and highly reversible Zn plating/stripping, delivering stable Zn|Zn symmetric-cell cycling for approximately 2500 hours. Furthermore, Zn|V_2O_5 full cells demonstrate excellent cycling stability at both low and high current densities, highlighting the effectiveness of the dual-plasticizer approach under practical operating conditions. This work establishes dual-plasticizer engineering as a simple and versatile strategy for simultaneously improving ion transport and Zn/electrolyte interfacial stability, offering new insights into the rational design of high-performance GPEs for durable AZIBs.

Data availability statement

All data generated or analyzed during this study are included in this published article (and its Supplementary Information files).

Funding

No funding was received for conducting this study.

References

1. Zhu, J., Tie, Z., Bi, S. & Niu, Z. Towards More Sustainable Aqueous Zinc-Ion Batteries. *Angew. Chemie* **136**, (2024).

2. Xu, H. *et al.* Advances in Aqueous Zinc Ion Batteries based on Conversion Mechanism: Challenges, Strategies, and Prospects. *Small* **20**, 1–37 (2024).

3. Fang, G., Zhou, J., Pan, A. & Liang, S. Recent Advances in Aqueous Zinc-Ion Batteries. *ACS Energy Lett.* **3**, 2480–2501 (2018).

4. Kakoty, B. *et al.* Decoding the Three-Card Monte: Unraveling the Role of Solvation Shell,

Surface Adsorption, and SEI Formation on Zn Anode Performance. *Chem. Mater.* **37**, 2907–2919 (2025).

5. Rana, A. *et al.* An Electroanalytical Perspective on the Competitive Interplay between Zinc Deposition and Hydrogen Evolution in Aqueous Zinc Metal Batteries. *Adv. Energy Mater.* **16**, 1–18 (2026).

6. Qi, R. *et al.* Gel Polymer Electrolyte toward Large-Scale Application of Aqueous Zinc Batteries. *Adv. Funct. Mater.* **33**, 1–34 (2023).

7. Jia, R. *et al.* Biopolymer-Based Gel Electrolytes for Advanced Zinc Ion Batteries: Progress and Perspectives. *Adv. Funct. Mater.* **35**, 1–28 (2025).

8. Rayung, M. *et al.* Bio-Based Polymer Electrolytes for Electrochemical Devices: Insight into the Ionic Conductivity Performance. *Materials (Basel).* **13**, 838 (2020).

9. Ling, H. Y. *et al.* Sustainable bio-derived materials for addressing critical problems of next-generation high-capacity lithium-ion batteries. *Materials Chemistry Frontiers* vol. 5 5932–5953 at https://doi.org/10.1039/d1qm00255d (2021).

10. Han, X. *et al.* From nature, requite to nature: Bio-based cellulose and its derivatives for construction of green zinc batteries. *Chem. Eng. J.* **454**, 140311 (2023).

11. Ganguly, S., Bennada, D. & Puravankara, S. Design and Evaluation of Carboxymethyl Cellulose-Starch Hybrid Gel Electrolytes Toward Quasi-Solid-State Zinc-Ion Batteries. *2025 IEEE 4th Int. Conf. Smart Technol. Power, Energy Control. STPEC 2025 - Conf. Rep.* 1–4 (2025) doi:10.1109/STPEC66316.2025.11490671.

12. Zheng, J. *et al.* Progress in Gel Polymer Electrolytes for Sodium-Ion Batteries. *ENERGY*

Environ. Mater. **6**, 1–29 (2023).

13. Gong, L., Najar, A. Al & Phan, A. Effect of Plasticizers on Performance in Single-Ion Conducting Polymer Electrolytes: Implications for Lithium-Ion Batteries. *Energy & Fuels* **40**, 9105–9114 (2026).

14. Deng, K. *et al.* Single-ion conducting gel polymer electrolytes: design, preparation and application. *J. Mater. Chem. A* **8**, 1557–1577 (2020).

15. Zuo, X. *et al.* Enhanced performance of a novel gel polymer electrolyte by dual plasticizers. *J. Power Sources* **239**, 111–121 (2013).

16. Liu, W., Zhang, X. K., Wu, F. & Xiang, Y. A study on PVDF-HFP gel polymer electrolyte for lithium-ion batteries. *IOP Conf. Ser. Mater. Sci. Eng.* **213**, 012036 (2017).

17. Gohel, K. & Kanchan, D. K. Effect of PC:DEC plasticizers on structural and electrical properties of PVDF–HFP:PMMA based gel polymer electrolyte system. *J. Mater. Sci. Mater. Electron.* **30**, 12260–12268 (2019).

18. Gohel, K., Kanchan, D. K., Machhi, H. K., Soni, S. S. & Maheshwaran, C. Gel polymer electrolyte based on PVDF-HFP:PMMA incorporated with propylene carbonate (PC) and diethyl carbonate (DEC) plasticizers : electrical, morphology, structural and electrochemical properties. *Mater. Res. Express* **7**, 025301 (2020).

19. Epure, V., Griffon, M., Pollet, E. & Avérous, L. Structure and properties of glycerol-plasticized chitosan obtained by mechanical kneading. *Carbohydr. Polym.* **83**, 947–952 (2011).

20. Ben, Z. Y., Samsudin, H. & Yhaya, M. F. Glycerol: Its properties, polymer synthesis, and

applications in starch based films. *Eur. Polym. J.* **175**, 111377 (2022).

21. Ganguly, S. & Puravankara, S. Sustainable, dendrite-suppressing, and robust citric acid cross-linked carboxymethyl cellulose-based quasi solid-state electrolyte for zinc-ion batteries. *J. Power Sources* **642**, 237005 (2025).

22. Zheng, Z. *et al.* An ultrathin natural cellulose based hydrogel membrane for the high-performance quasi-solid-state zinc-ion batteries. *Chem. Eng. J.* **475**, 146314 (2023).

23. Huang, S., Hou, L., Li, T., Jiao, Y. & Wu, P. Antifreezing Hydrogel Electrolyte with Ternary Hydrogen Bonding for High-Performance Zinc-Ion Batteries. *Adv. Mater.* **34**, (2022).

24. Lin, X. *et al.* Super-tough and self-healable all-cellulose-based electrolyte for fast degradable quasi-solid-state supercapacitor. *Carbohydr. Polym.* **304**, 120502 (2023).

25. Qiu, T. *et al.* Rapidly Synthesized Single-Ion Conductive Hydrogel Electrolyte for High-Performance Quasi-Solid-State Zinc-ion Batteries. *Angew. Chemie Int. Ed.* **62**, (2023).

26. Şensoy Gün, B. & Yontar, A. K. Lignocellulosic almond shell nanocomposites embedded with biogenic iron oxide nanoparticles: structural and antibacterial properties. *Cellulose* (2026) doi:10.1007/s10570-026-07145-6.

27. Dueramae, I., Okhawilai, M., Kasemsiri, P. & Uyama, H. High electrochemical and mechanical performance of zinc conducting-based gel polymer electrolytes. *Sci. Rep.* **11**, (2021).

28. Dhanush, P. C. & Ismayil. Ionic transport and structural analysis of zinc chloride doped ί-carrageenan solid polymer electrolytes for energy storage devices. *J. Energy Storage* **145**,

119933 (2026).

29. Adam, A. A. *et al.* Insight into the Effect of Glycerol on Dielectric Relaxation and Transport Properties of Potassium-Ion-Conducting Solid Biopolymer Electrolytes for Application in Solid-State Electrochemical Double-Layer Capacitor. *Molecules* **28**, (2023).

30. Capanema, N. S. V. *et al.* Superabsorbent crosslinked carboxymethyl cellulose-PEG hydrogels for potential wound dressing applications. *Int. J. Biol. Macromol.* **106**, 1218–1234 (2018).

31. Dong, Y. *et al.* Spontaneous anode-molecule interface triggers highly reversible zinc anode. *Energy Storage Mater.* **70**, 103465 (2024).

32. Li, G. *et al.* A biocompatible electrolyte enables highly reversible Zn anode for zinc ion battery. *Nat. Commun.* **14**, 6526 (2023).

33. Huang, C. *et al.* Self-Healing SeO2 Additives Enable Zinc Metal Reversibility in Aqueous ZnSO4 Electrolytes. *Adv. Funct. Mater.* **32**, (2022).

34. Liang, F. *et al.* Electrochemical Activation in Vanadium Oxide with Rich Oxygen Vacancies for High-Performance Aqueous Zinc-Ion Batteries. *ACS Sustain. Chem. Eng.* **12**, 5117–5128 (2024).

Legends

Figure legends

Figure 1: Structural, morphological, and thermal evolution of CMC-based gel polymer electrolytes: (a) Schematic illustration of the fabrication process of the CMC-based GPEs containing different PC and glycerol compositions (PG00, PG10, PG11, and PG01); (b) Three-dimensional AFM surface topography of PG11 membrane; (c) XRD patterns of the GPEs; TG and DTG curves of (d) PG00, (e) PG10, (f) PG11, and (g) PG01.

Figure 2: Tensile behavior and mechanical flexibility of CMC-based GPEs: Tensile behavior and mechanical flexibility of CMC-based GPEs: Mechanical properties of the GPE membranes. (a) Representative stress-strain curves of PG00, PG10, PG11, and PG01; (b) Comparison of the tensile strength and elongation-at-break of the prepared GPE membranes.

Figure 3. **Enhanced ion transport kinetics and electrochemical window of GPEs:** (a) Electrolyte uptake of PG00, PG10, PG11, and PG01 after soaking in 3 M $ZnSO_4$ electrolyte; (b) Ionic conductivity of the prepared GPEs at room temperature; (c) Zn^{2+} transference number measurements of PG00 and PG11 using the Bruce–Vincent method; (d) Chronoamperometric response of Zn|Zn symmetric cells at a polarization of -100 mV, illustrating the Zn^{2+} diffusion behavior in PG00 and PG11; (e) LSV of Zn|SS cells at a scan rate of 0.5 mV s^{-1}.

Figure 4. **Reversibility and interfacial kinetics of Zn plating/stripping:** (a) Long-term Zn plating/stripping performance of Zn|Zn symmetric cells using PG00 and PG11 at 1 mA cm^{-2} with an areal capacity of 1 mAh cm^{-2}; Zn nucleation overpotential of Zn|Cu cells during the 1st, 100th, and 200th plating cycles at 1 mA cm^{-2} and 1 mAh cm^{-2} for (b) PG00, and (c) PG11; EIS spectra

of Zn|Cu cells measured under (d) OCV; and (e) an applied bias corresponding to the initial Zn nucleation overpotential.

Figure 5. **Morphological evolution, transport mechanism, and full-cell performance of GPEs:** Post-cycling SEM images of Zn anodes retrieved from Zn|Zn symmetric cells after 200 cycles, using (a) PG00, and (b) PG11; (c) Proposed Zn^{2+} transport mechanism in the dual-plasticized GPE; Cycling performance and coulombic efficiency of Zn|V_2O_5 full cells with the PG11 electrolyte at (d) 0.1 A g^{-1}, and (e) 1 A g^{-1}.

Table legend

Table 1: Formulation and plasticizer ratios of CMC-based GPEs.: GPE membrane compositions for the as-synthesized GPEs with varying PC and glycerol ratios.

Author information

Corresponding author:

Sreeraj Puravankara: School of Energy Science and Engineering, Indian Institute of Technology Kharagpur, Kharagpur, West Bengal-721302, India; https://orcid.org/0000-0002-9238-0148; Phone: +913222 26080; Email: sreeraj@iitkgp.ac.in

Authors:

Sreshtha Ganguly: School of Energy Science and Engineering, Indian Institute of Technology Kharagpur, Kharagpur, West Bengal-721302, https://orcid.org/0009-0008-6561-2362; Email: gangulysreshtha@kgpian.iitkgp.ac.in

Dilip Bennada: School of Energy Science and Engineering, Indian Institute of Technology Kharagpur, Kharagpur, West Bengal-721302; Email: bennadadilip.24@kgpian.iitkgp.ac.in

Amrit Choudhury: School of Energy Science and Engineering, Indian Institute of Technology Kharagpur, Kharagpur, West Bengal-721302; Email: amritchoudhury98@gmail.com

Author Contributions Statement

S.G. contributed to Conceptualization, Methodology, Investigation, Visualization, Formal analysis, Software, and Writing - original draft, review & editing.

D.B.- Methodology, Investigation

A.C.- Software

S.P. contributed to Supervision, Visualization, Resources, Writing - review & editing, and Project Administration.

Additional Information

Competing Interests

The authors declare no competing interests.

Acknowledgments

SG and AC acknowledge IIT Kharagpur for the doctoral fellowships. The authors gratefully acknowledge Dr. Kingshuk Roy (RISE, TCG CREST, Kolkata) for his valuable discussions and assistance with the electrochemical measurements.

Supplementary Files

This is a list of supplementary files associated with this preprint. Click to download.

- SupportingInformation.pdf